https://doi.org/10.1016/j.actbio.2021.05.034

Plasmonic-Doped Melanin-Mimic for CXCR4-Targeted NIR-II Photoacoustic Computed Tomography-Guided Photothermal Ablation of Orthotopic Hepatocellular Carcinoma

Shuo Qi[†,§,‡,⊥,||], *Yachao Zhang*[§,‡,||], *Gongyuan Liu*[¶,||], *Jiangbo Chen*[§,‡], *Xiaozhen Li*[¶], *Yuqi Yang*[°], *Jiahai Shi*[°], *Chun-Sing Lee*[¶], *Guangyu Zhu*[*,¶], *Puxiang Lai*[*,¤,+], *Lidai Wang*[*,§,‡], *Chihua Fang*[*,†,⊥]

[†]Department of Hepatobiliary Surgery, Zhujiang Hospital, Southern Medical University, Guangzhou, 510280, China.

[§]City University of Hong Kong Shenzhen Research Institute, Shenzhen, 518057, China.

[‡]Department of Biomedical Engineering, City University of Hong Kong, Hong Kong SAR, China.

[¶] Center of Super-Diamond and Advanced Films and Department of Chemistry, City University of Hong Kong, Hong Kong SAR, China.

[°]Department of Biomedical Sciences, College of Veterinary Medicine and Life Sciences, City University of Hong Kong, Hong Kong SAR, China.

[¤] Department of Biomedical Engineering, The Hong Kong Polytechnic University, Hong Kong SAR, China

[+] The Hong Kong Polytechnic University Shenzhen Research Institute, Shenzhen, 518057, China.

[⊥]Guangdong Provincial Clinical and Engineering Center of Digital Medicine, Guangzhou, 510280, China.

[||]These authors contributed equally to this work.

*Address correspondence to:
guangzhu@cityu.edu.hk
puxiang.lai@connect.polyu.hk
lidawang@cityu.edu.hk
fangch_dr@163.com

ABSTRACT: Effective and non-invasive diagnosis and prompt treatment of early-stage hepatocellular carcinoma (HCC) is highly demanded to lower its mortality rate. Herein, the integration of high-resolution diagnostic NIR-II photoacoustic computed tomography (PACT) and imaging-guided targeted photothermal ablation of orthotopic small HCC (SHCC) is presented for the first time, which is enabled by a plasmonic platinum (Pt^0) doped polydopamine melanin-mimic nano-agent. As designed, antibody-modified nano-agent (named as Pt@PDA-c) with plasmonic blackbody-like NIR absorption and superior photothermal conversion efficiency (71.3%) can selectively target and kill CXCR4-overexpressed HCC (HepG2) cells, which was validated in the *in vitro* experiments. With real-time quantitative guidance by PACT for accurate diagnosis of intraabdominal SHCC (about 4 mm depth), effective noninvasive photothermal ablation of SHCCs was successfully implemented on an orthotopic tumor-bearing mice model without damaging adjacent liver tissues. These results promise great potential of NIR-II PACT-guided non-invasive photothermal therapy as an innovative photo-theranostic approach and expand the biomedical applications of melanin-mimic materials.

KEYWORDS: small hepatocellular carcinoma, melanin-mimic, second near-infrared (NIR-II), photoacoustic imaging, photothermal therapy.

INTRODUCTION

Hepatocellular carcinoma (HCC) is one of the deadliest cancers worldwide with 5-year survival rate being less than 18%.[1,2] Most HCC cases were diagnosed at advanced stages, leading to malignant tumor growth and metastasis, and high mortality rate.[3, 4] Due to insufficiency in either sensitivity or penetration depth, early diagnosis of small HCC is still clinically challenging. X-ray computed tomography (CT), magnetic resonance imaging (MRI), and ultrasound (US) imaging can image solid tumors deep

within tissue. However, their sensitivities are insufficient to detect millimeter-sized small HCC lesions.[5-8] Optical imaging has attracted tremendous attention for its biosafety, superior sensitivity, and molecular imaging ability, but cannot offer high resolution in deep tissue.[9-10]

Via combining optical excitation and ultrasonic detection, photoacoustic imaging (PAI) can acquire high-resolution images in deep tissue with an excellent sensitivity of endogenous and exogenous contrasts, such as hemoglobin concentration, oxygen saturation, lipid, DNA/RNA, and various molecular and nano-agents.[11-17] Especially, the second near-infrared (NIR-II, 1000-1350 nm) optical window allows the excitation laser to reach deeper tissue lesions, significantly increasing the penetration depth of optical imaging, which is favorable for deep small HCC (SHCC, diameter within 5 mm) detection.[18-24] On the other hand, as some photoacoustic contrast agents have high photothermal conversion efficiency, photothermal therapy (PTT) can be readily integrated with real-time photoacoustic guidance, offering a non-invasive and efficient theranostic approach for SHCC.

That said, limited types of NIR-II agents are available for diagnosis and photothermal therapy of SHCC. To date, most NIR-II photoacoustic contrast agents, such as heptamethine or benzothiadiazole dyes, semi-conductive conjugated polymers, or plasmonic noble metal (Au, Pt, or Pd) nanoparticles, have uncertain long-term retention-related systemic toxicity, hindering clinical translations.[25-30] Inspired by label-free melanoma photo-theranostics, melanin (natural extract or synthetic) derivatives are proven to be excellent PTT agents and drug delivery nanoplatforms with superior biocompatibility compared to full-metallic nano-agents.[31-34] Nonetheless, melanin- or synthetic polydopamine (PDA)-based agents share an intrinsic defect of low NIR-II absorption (over 1000 nm) and thus are not suitable for orthotopic tumor diagnosis and therapy in deep tissue.[35-38]

Here, we develop a new targeted plasmonic-modified melanin-based nano-agent for NIR-II photoacoustic guidance and photo-theranostics of early primary HCC (Scheme 1). Via encapsulation of doping amount (2.7%) of plasmonic Pt^0 into PDA nanoparticles, a blackbody-like novel NIR-II photothermal agent was obtained with an outstanding photothermal conversion efficiency of 71.3% (at 1064 nm optical wavelength). Further by surface modification of sulphydryl polyethylene glycol (PEG-SH) and CXCR4 antibody, an HCC targeting melanin mimic nano-agent was obtained (namely Pt@PDA-c). CXCR4 is associated with microvascular invasion (MVI) during

the development of HCC with highly carcinoma cell-specific expression, which promises the selectivity of HCC targeting. Pt@PDA-c-mediated NIR-II photoacoustic computed tomography (PACT) has deep tissue penetration and high spatial resolution, and can accurately locate orthotopic SHCC lesions. After treatment, Pt@PDA-c can be excreted from the metabolic organs within 48 hours. *In vivo* experiments show that PTT can ablate SHCC with no reoccurrence and minimal damage to healthy liver tissue. Besides real-time guidance for PTT, PACT with high tumor-selectivity and accuracy can also verify the metabolic clearance of Pt@PDA-c from mean organ and regression of tumor lesion. For the first time, we successfully achieved a noninvasive diagnosis by NIR-II high-resolution PACT and targeted ablation by PTT against SHCCs on orthotopic tumor-bearing mice model, which reveals a novel and potent theranostic approach towards SHCC treatment.

METHODS AND EXPERIMENTS

Synthesis of Pt@PDA-c NPs

First, an aqueous solution of dopamine hydrochloride (5 mg mL^{-1}, 3 mL) was added into 0.2 M $NaHCO_3$-HCl buffer (25 mL, pH 8.2). After 5 min, 5-mL K_2PtCl_4 solution (1 mg mL^{-1}) was injected into the above solution and kept at room temperature for 8 hours. Then, the solid product was collected via centrifuging at 10,000× gravity and washed 3 times with deionized (DI) water. The obtained nanoparticles were dispersed in 2-mL DI water via sonication, then injected into 10-mL PEG-SH solution (2 mg mL^{-1}), and kept for PEG capping for 24 hours. After that, anti-CXCR4 (20 μg mL^{-1}) was added to the latest particle suspension, and stirred for 12 hours in dark. At last, the dispersion was centrifuged and washed with DI water several times, and then lyophilized to obtain black solid powder of Pt@PDA-c nanoparticles. To analyze the Pt amount, 4.5-mg freeze-dried sample was fully digested. The Pt amount was tested with ICP-OES and calculated to be 2.71±0.08 %.

MTT dark toxicity assay

Methyl thiazolyl tetrazolium (MTT) cell viability assay was performed to evaluate the dark cytotoxicity of Pt@PDA-c NPs. HepG2 cells and LO2 cells (5,000 cells per well, 200 μL) were seeded in a respective 96-well plate and cultured for 24 hours. The medium was then replaced with a mixture of culture medium containing varying concentrations of NPs (0, 0.06, 0.13, 0.25, and 0.5 mg mL^{-1}) and incubated in the dark

for another 24 hours. The MTT was added (150 μL per well) into each test well after removing the mixture and incubated for 3 hours, then the MTT in each well was replaced with 150 μL dimethyl sulfoxide (DMSO). The absorbance in each well at 570 nm was measured by a microplate reader (Molecular Devices, USA). All experiments were repeated three times and the results were averaged.

Cellular Targeting Uptake of Pt@PDA-c NPs

To verify the targeted uptake of Pt@PDA-c NPs by HepG2 cells, a lab-built optical-resolution photoacoustic microscopy (OR-PAM) system (Figure S2, Supporting Information) was used to conduct the PA imaging of the HepG2 and LO2 cells.[39] Moreover, a laser scanning confocal microscope (Leica, Germany) was applied to further verify the active targeting uptake by human HCC cancer cells. Detailed experimental procedures of PA imaging and cell confocal imaging are shown in the Supporting Information.

***In vitro* PA imaging**

The Pt@PDA-c NPs aqueous solution at different concentrations (0, 0.1, 0.2 0.3, 0.4, 0.5 and 0.6 mg mL^{-1}) were sealed into different rubber capillary tubes beforehand. Then a lab-built photoacoustic computed tomography (PACT) system (Figure S1, Supporting Information) was used to detect and quantify the PA signal for each sample at 1064 nm.[40] Meanwhile, a capillary tube filled with Pt@PDA-c (0.5 mg mL^{-1}) was prepared to perform the PA imaging at different optical wavelengths (664, 764, 864, 964, 1064, and 1100 nm). To measure the penetration depth of PA imaging at NIR-I (764 nm) and NIR-II (1064 nm) window, few pieces of sliced chicken breast tissue samples were covered onto a polyethylene tube filled with Pt@PDA-c (0.25 mg mL^{-1}) and the PA signals were collected from the top of the tissue.

***In vitro* NIR-II PTT**

The Pt@PDA-c NPs aqueous solution in different concentrations (0, 0.06, 0.13, 0.25 and 0.33 mg mL^{-1}) were loaded to quartz cuvettes. The sample in each tube was irradiated by 1064-nm laser (1 $W \cdot cm^{-2}$) for 10 minutes, and the temperature change was detected by a FLIR thermal camera. The sample dispersions were irradiated with the 1064-nm laser until the temperature reached equilibrium, then the laser was turned off

and the sample naturally cooled to the room temperature. This procedure was repeated by 3 cycles. The temperature variation was recorded every 30 seconds. The HepG2 cells (5,000 cells per well) were seeded in a 96-well plate and cultured for 24 hours (37°C, 5% CO_2). The culture medium was replaced with NPs-containing medium (0, 0.06, 0.13, 0.25, 0.33 and 0.5 mg mL^{-1}, 150 μL per well), and the cells were incubated for 4 hours. The cells were irradiated by 1064-nm laser at 1 $W \cdot cm^{-2}$ for 10 minutes and then incubated without irradiation for another 4 hours. The cell viability was tested by MTT assay. Meanwhile, following the same cell culture process, the HepG2 cells (1×10^5 cells per dish) were seeded in four confocal dishes and set up laser groups (NPs +laser and PBS +laser) and no laser groups (NPs and PBS). Subsequently, in the laser groups, the cells were irradiated with 1064-nm laser at 1 $W \cdot cm^{-2}$ for 10 minutes and then incubated without irradiation for another 4 hours. The *in vitro* PTT outcomes was examined with a fluorescence microscope after staining the sample with Calcein-AM and PI for 15 minutes.

In vivo and *ex vivo* NIR-II PA imaging

Orthotopic tumor-bearing BALB/c nude mice were used in *in vivo* PA imaging. After anesthesia, the Pt@PDA-c NPs (30 $mg \cdot kg^{-1}$ body weight) were injected into the tumor-bearing mice via the tail vein. To detect the accumulation time of Pt@PDA-c NPs in the orthotopic tumors, the PACT system at 1064 nm was applied to image the mice at different times after injection (0, 1, 3, 4, 5, 6, 12, and 24 hours). To confirm the accumulation of Pt@PDA-c NPs in the orthotopic tumors, a laparotomy was carried out in mice, and the tumors and major organs (heart, liver, spleen, lungs, and kidneys) were excised at the time point above. Then the excised tumors and organs were imaged by the PACT system at 1064 nm. Moreover, to assess the sensitivity of NIR-II PA imaging for tumor therapy, the PA imaging of the tumor was performed at the previously confirmed NPs accumulation time before and after the tumor resection. To verify the clearance ability of Pt@PDA-c NPs in mice, the *ex vivo* quantification of PA signals (1064 nm) of the major organs in the experimental group were detected by the PACT system after tail vein injection of NPs (30 $mg \cdot kg^{-1}$ body weight) at different time points (24, 36, and 48-hours post-injection).

In vivo NIR-II PTT

Orthotopic tumor bearing mice were used to complete the NIR-II PTT experiments

in vivo. The mice were categorized to laser treatment groups (L +NPs and L +PBS) and no laser groups (NPs and Control). In the laser treatment groups, the Pt@PDA-c NPs (30 $mg \cdot kg^{-1}$ body weight) or PBS (200 μL) were injected intravenously before laser irradiation. In the no laser groups, the same amount of Pt@PDA-c was injected into the NPs group while the Control group had no injection. The location of the tumor was confirmed with bioluminescence imaging and the NIR-II PA imaging. Then the 1064-nm laser was used to irradiate the tumor site of the laser groups (1 $W \cdot cm^{-2}$, 10 minutes) and the temperature was recorded using a FLIR thermal camera during irradiation. The bioluminescence imaging in the laser treatment group was detected by a Bruker *in vivo* Xtreme live animal imaging system on days 8 and 16 post-treatment. The body weights in all groups were measured and recorded every other day. After 17 days post-treatment, all mice were executed by cervical dislocation, and the tumors and major organs were harvested for further analysis.

Histopathology test

After the PTT treatment, the tumors from all groups were stained with Hematoxylin and Eosin (H&E) for histopathology examination. The major organs, including heart, liver, spleen, lung, and kidney, were stained with H&E for histopathology examinations to further evaluate biosafety of Pt@PDA-c.

RESULTS AND DISCUSSION

As illustrated in Scheme 1, via doping of Pt and surface modification of CXCR4-antibody, the synthetic polydopamine-based melanin-mimic nano-agent was obtained for photoacoustic and photothermal applications. The TEM image shows that the size of Pt@PDA-c is around 150 nm (Figure 1A), which is close to the size of 140.5 ±31.7 nm tested via DLS (Figure 1B). The changes in the zeta potential of PEG-modified Pt@PDA (-38.4 ±6.2 mV) and Pt@PDA-c (-33.5 ±5.4 mV) indicate successful electrostatic adsorption of the positively charged CXCR4 antibody (Figure S3, Supporting Information), which can be also validated by fluorescence spectra because the antibody was labelled with FITC (Figure S4, Supporting Information). The UV-Vis-NIR spectra of PDA and Pt@PDA-c (Figure 1C) indicates that Pt@PDA-c is a typical plasmonic blackbody-like material with a broadband absorption from 500 to 1100 nm without specific absorption peak and follows linear concentration-absorption

relationship (Figures 1D and S5 in Supporting Information), while PDA exhibits a drastic decrease of absorption with increased wavelength. Different from the reaction between $HAuCl_4$ and dopamine, the Pt doping amount was controlled below 3%, even with a further increase of mass feeding ratio of K_2PtCl_4 to dopamine (from 1:3 to 1:2 or 1:1).[38] This phenomenon is attributed to the relatively lower redox potential of K_2PtCl_4 (+0.758 V *vs* SHE) than that of $HAuCl_4$ (+0.93 V *vs* SHE) precursors, which limits the reaction progress and leads to the doping of Pt in PDA nanostructure.[41] The size of Pt@PDA-c NPs remains stable in 2 weeks for long-term storage at room temperature (Figure S6, Supporting Information). The NPs disperse well in physiological conditions (DMEM and FBS) and shows excellent stability for 2 weeks of incubation (Figure S7, Supporting Information). In summary, Pt@PDA-c has proper particle size, broadband NIR-II absorption, and excellent stability.

The NIR-II photothermal performance of Pt@PDA-c NPs was further investigated. With laser irradiation, the temperature (Figure 1e and 1g) of NPs aqueous solution changes with different concentrations (0, 0.06, 0.13, 0.25 and 0.33 mg mL^{-1}). For the solution with a concentration of 0.33 mg mL^{-1}, the temperature increases from 25 °C to 52.5 °C after irradiation for 10 minutes (1064 nm, 1 $W \cdot cm^{-2}$). By contrast, the temperature of water only increases by 6.9 °C under the same irradiation condition. Besides, the photothermal stability of NPs (0.25 mg mL^{-1}) was confirmed by the heating-and-cooling stability test (Figure 1f). Pt@PDA-c NPs presents great stability, and its temperature change has no noticeable attenuation over three cycles of heating and cooling. As presented in Figures 1h, the photothermal conversion efficiency (PCE) of Pt@PDA-c was 71.3 % (calculated from a reported method in Supporting Information) and was superior among the state-of-the-art organic and inorganic materials (Figure S8, Supporting Information).[26,39,42-50] Therefore, Pt@PDA-c with a high PCE and excellent photothermal stability encourage further *in vitro* and *in vivo* PTT assays.

Pt@PDA-c NPs have enhanced NIR absorption and are ideal for NIR-II PA imaging. To verify this, the PACT system was used to image Pt@PDA-c NPs *in vitro*. Figure 2a presents the PA intensity of NPs aqueous solution samples with gradually increased concentrations (0~0.6 mg mL^{-1}). Quantitative analysis proves that the PA magnitude is proportional (R^2= 0.9829) with the NPs concentration at 1064-nm wavelength and 8 $mJ \cdot cm^{-2}$ fluence (Figure 2b). Meanwhile, the NPs (0.5 mg mL^{-1}) present excellent photostability with no obvious PA signal or absorption spectrum changes after intensive

exposure with a 1064-nm laser (20 pulses per second, 8 $mJ \cdot cm^{-2}$ fluence) for 1000 seconds (Figures 2c, 2d and S9 in Supporting Information). To verify the PA performance of Pt@PDA-c at different wavelengths in the NIR window, the PA imaging was performed at different wavelengths (664, 764, 864, 964, 1064, and 1100 nm) at an intensity of 8 $mJ \cdot cm^{-2}$ (Figures 2e and 2f). With superior PA signal and photostability, Pt@PDA-c is a promising biological imaging contrast agent *in vivo*.

To demonstrate that NIR-II PA imaging has deep penetration, the NIR-I (764 nm) and NIR-II (1064 nm) PA penetration depths were compared with the same surface fluence of 9.5 $mJ \cdot cm^{-2}$. PA signals were collected from the top of the polyethylene tube covered with different thicknesses of chicken breast tissue (setup presented in Figure S10 in Supporting Information). As shown in Figure 2g, the PA signal can be distinctly detected at the thickness of 36 mm at 1064 nm, but scarcely detected at 764 nm. Quantitative PA signal at 1064 nm is significantly higher than the one at 764 nm with various thicknesses of chicken breast (Figure 2h). Similar conclusions were made in other reports, suggesting that NIR-II PA imaging possesses great potential to be further applied to the orthotopic HCC tumor model at depths *in vivo*.[18-19,51]

As reported,[52-54] the CXCR4 protein was highly expressed on cell membranes and cytoplasm of human HCC cell lines, including HepG2 cells, but of very low expression level in normal human hepatocyte LO2 cells, which was also verified by confocal laser scanning microscopy (CLSM) experiment (Figure S11, Supporting Information). Therefore, CXCR4 modified Pt@PDA-c can be actively ingested by HepG2 cells, rarely by LO2 cells. Figure 3a presents the carcinoma cell-targeted uptake ability of Pt@PDA-c NPs imaged with optical-resolution photoacoustic microscopy (OR-PAM). After incubating with the cells for 4 hours, obvious PA signals were detected from the aggregated NPs in the HepG2 group, but not from the LO2 group. Quantitative data displayed in Figure 3b indicates that the HepG2 cells have a higher PA intensity than the LO2 cells, and the difference is statistically significant (p-value =0.00015). For further confirmation, the CLSM imaging was performed to verify the targeted cellular uptake ability of Pt@PDA-c NPs, which presents an identical result with OR-PAM (Figure 3c). The OR-PAM and CLSM imaging of the HepG2 cells were also carried out after incubation with Pt@PDA-c NPs for 1 and 2 hours (Figures S12 and S13 in Supporting Information). The result indicates a gradually increased uptake of NPs in the cells with longer incubation time. These results show that Pt@PDA-c has a superior uptake efficiency by HepG2 cells and thus is suitable for PA detection and theranostics

of SHCC.

To verify the biosafety of doping amount of Pt within Pt@PDA-c NPs, a dark toxicity assay was carried out before *in vivo* experiments. The result indicates that the HepG2 and LO2 cells remained viable above 91.9 % and 94.0 %, respectively, after incubated for 24 hours with a high concentration of Pt@PDA-c NPs (0.5 mg mL^{-1}), indicating negligible cytotoxicity without laser radiation (Figures 3d and 3e). Then a cell-based phototoxicity assay was carried out to verify the PTT performance of Pt@PDA-c NPs under NIR-II laser irradiation (1064 nm, 1 $W \cdot cm^{-2}$, 8 min). As illustrated in Figure 3e, with increased concentration of Pt@PDA-c, the relative viability of HepG2 cells gradually decreased, and the cell viability declined to 7.8 % after laser irradiation at the concentration of 0.5 mg mL^{-1}. The Calcein-AM (show in green, indicating live cells) and propidium iodide (PI, shown in red, dead cells) co-staining tests were performed to visually present the hyperthermia cell-killing effect by Pt@PDA-c NPs. The results were presented in Figure 3f. The strong green fluorescence signals are detected in cells treated with PBS, PBS +laser, and NPs, but strong red fluorescence signals are observed in the NPs +laser group, indicating the dead cells with a permeable membrane to be stained with PI. As a result, laser exposure of a safe intensity can induce effective PTT of HepG2 cells with the help of Pt@PDA-c. Supported by excellent biosafety, and prompt cancer cell killing via PTT, Pt@PDA-c is proven to be an excellent HCC-specific PTT agent.

Pt@PDA-c NPs (30 $mg \cdot kg^{-1}$ body weight) were injected into orthotopic SHCC bearing nude mice. The mice were monitored in real-time using the NIR-II PACT system in the following 24 hours (Figure S14, Supporting Information). As presented in Figures 4a and 4b, the accumulation of NPs in the tumor peaks at ~4 hours post-injection. The schematic diagram of the PA imaging setup was shown in Figure S15a (Supporting Information). The depth of the orthotopic tumors is about 4 mm beneath the skin of abdomen (Figures S15b and S15c, Supporting Information). To further verify the accumulation of the NPs, the resected tumors and other major organs, including heart, liver, spleen, lungs, and kidneys, were imaged and quantified at the time point of 4 hours post-injection (Figures 4c and 4d). These results suggest that the tumor generate much stronger PA signals than that in other major organs do, which indicates the targeted gathering of the NPs in the orthotopic tumor of mice. The liver tissue of other normal liver lobes with low-level PA signal indicates the low accumulation level of NPs in the normal liver region, which proves the excellent active

targeting ability of Pt@PDA-c NPs. Noteworthily, the spleen generates a stronger signal than other organs. The possible reason is that the NPs were engulfed by macrophages as a part of the excretion pathway which has been confirmed in other studies.[55-56] The result indicates that Pt@PDA-c can successfully assist PACT for sensitive and accurate SHCC detection (in particular, for tumor diameter within 5 mm and depth about 4mm) through the active tumor homing effect.

Because the tumor edge can be identified by PACT with NPs labeling, surgical resection guided by PACT can be conducted. To validate the tumor therapy in orthotopic SHCC bearing mice, the PA images of the tumor region were acquired before and after surgical resection. As presented in Figures 4e and S16 (Supporting Information), the NPs accumulation was detected in the tumor region. The tumor location was also verified by exploratory laparotomy. After tumor excision and abdominal suture, PA signal disappeared in the original tumor region. H&E staining results further confirmed the excisional tumor. However, facing the risk of severe trauma after surgery, non-invasive therapy, *i.e.*, PTT, is preferred for early-stage SHCC treatment. Pt@PDA-c-assisted PACT is sensitive to guide and evaluate the effectiveness of PTT for SHCC.

To further verify the metabolic body clearance of NPs *in vivo*, the biodistribution in major organs (heart, liver, spleen, lung, and kidney) was detected after intravenous injection at 24, 36, and 48 hours. As a control, the same amount of saline was injected to another group of mice to detect the basic PA signals of the organs. Figure 4f shows that the relative PA signals from major organs gradually decreased after 24 hours post-injection and vanished in 2 days compared with the control group. With efficient tumor targeting and metabolic clearance, we conclude that Pt@PDA-c is an effective contrast agent for PA-guided tumor diagnosis and therapy *in vivo*.

The SHCC tumor formation was confirmed by bioluminescence 10 days after HepG2 cells implantation. Guided by PA imaging, the PTT was carried out in the orthotopic HCC bearing nude mice (n=3 in each group) at 4-hours post-injection. The orthotopic tumors were revealed by PACT and bioluminescence imaging before treatment. Then, PTT was conducted twice in two days. The detailed procedure of the treatment and evaluation was illustrated in Figure 5a. As shown in Figures 5b and 5c, the local temperature of the tumor site in the L +NPs group increased rapidly to 50 °C in 5 minutes under 1064-nm laser irradiation (1 $W \cdot cm^{-2}$) and stayed at this temperature for 5 minutes. This hyperthermia was enough for tumor ablation and meanwhile did not

exceed PTT temperature threshold to cause damage to healthy tissue. For comparison, the local tumor temperature of the L +PBS group increased to only 40 °C. Distinct tumor inhibition was observed in the L +NPs group but not in the L +PBS group. As presented in Figures 5d and S17 (Supporting Information), the PA signal of the tumor in the L +NPs group significantly decreased on day 8 after treatment and became obscure on day 16. Meanwhile, the bioluminescence imaging and the quantitative data also show much reduced bioluminescence from the tumor region in the L +NPs group, but increased bioluminescence from the L +PBS group (Figures 5e and S18 in Supporting Information). Because the bioluminescence was directly related to the viability of cancer cells, the bioluminescence result indicates that photothermal ablation of SHCC was successful. After PTT, the orthotopic tumors and other major organs were resected for H&E staining on day 17. Photographs and the H&E staining (Figures 5f and S19 in Supporting Information) of the tumor from the L +NPs group indicate remarkable tumor necrosis after PTT treatment, while the tumor in the L +PBS group shows no change before and after the treatment. Although similar studies have successfully conducted the PTT of SHCCs in mice, but the untargeted and invasive PTT may not be recommended in the coming epoch.[23,57-58] Targeted, non-invasive and effective PTT that we've implemented for the first time may change the clinical treatment decisions for SHCCs in the near future.

Minimal systemic damage is important for clinical transformation. In case the PTT treatment may cause any tissue denaturation or damage of the major organs, the body weight changes were recorded and H&E staining of the major organs were performed after treatment. The body weights in all groups were continuously monitored every two days during the subsequent 16 days (Figure S20, Supporting Information). No significant body weight loss and abnormal behaviors of treated mice (for example unusual physical movement, anorexia, or being aggressive/depressive) were observed in all groups throughout the treatment period. As mentioned above, clearance of Pt@PDA-c in all major organs were confirmed 2 days after injection *in vivo*. Moreover, the H&E staining of the major organs (heart, liver, spleen, lung, and kidney) in all groups were presented in Figure S21 (Supporting Information). No significant tissue denaturation or damage of the major organs occurred in all the groups, which proves the safety of Pt@PDA-c NPs and NIR-II laser during the whole treatment process. The encouraging theranostic outcome exhibits great potentials of Pt@PDA-c and the PA-guided PTT to treat SHCC in clinics.[59]

CONCLUSIONS

To conclude, plasmonic-doped, melanin-mimic, and polydopamine-based theranostic nanoparticles (Pt@PDA-c) are developed for early detection of small HCC with NIR-II PACT and efficient noninvasive photothermal ablation of orthotopic tumors. Attributed to the superior photothermal conversion efficiency, Pt@PDA-c exhibits potent cancer cell-killing *in vitro* and excellent biosafety. Via targeted tumor binding, PA imaging of SHCC was successfully conducted to detect millimeter-sized orthotopic HCCs using Pt@PDA-c as the contrast agent. Guided by real-time PA imaging, Pt@PDA-c-mediated PTT can eradicate SHCC without recurrence. Damage to health liver tissue was minimized due to the tumor-targeting effect and NIR-II laser irradiation. These results not only offer a new development of melanin derivative-based material for NIR-II PA imaging but also demonstrate a promising noninvasive PTT theranostic strategy for SHCC.

ASSOCIATED CONTENT

Supporting Information Available: The chemicals needed for the synthesis of Pt@PDA-c nanoparticles, facilities for characterizations, zeta potential, fluorescent spectra and stability of Pt@PDA-c, fundamental and schematic diagrams of PACT and OR-PAM systems, PCE calculation, cell lines and animal models, cell PA and CLSM imaging, photograph of the PA instrument, quantitative data of PA and bioluminescence signal in different treatment groups, photographs and volume of the tumor in groups, body weight changes and H&E staining of major organs from mice receiving different treatments (Figure S1-S21)

AUTHOR INFORMATION

Corresponding Authors

*E-mail: guangzhu@cityu.edu.hk

*E-mail: puxiang.lai@connect.polyu.hk

*E-mail: lidawang@cityu.edu.hk

*E-mail: fangch_dr@163.com

Author Contributions

C. Fang, L. Wang and P. Lai designed the project. G. Liu and G. Zhu developed the nano-agent. Y. Zhang, J. Chen and L. Wang developed the imaging system. S. Qi, Y. Zhang, X. Li, Y. Yang conducted the PAI and PTT experiments. S. Qi, Y. Zhang and G. Liu analyzed the data. The manuscript was written through contributions of all authors. All authors have given approval to the final version of the manuscript.

[||]S. Qi, Y. Zhang and G. Liu contributed equally to this work.

ACKNOWLEDGMENTS

This work was partially supported by the grants from the National Natural Science Foundation of China (81627805, 81930048, 22077108), University Grants Committee of Hong Kong SAR (No.11101618, 11215817, 11103320, R5029-19), the National Key R&D Program, China (No. 2016YFC0106500), the NSFC-GD Union Foundation, China (No. U1401254), National High Technology Research and Development Program of China (863 program, China) (No. 2006AA02Z346 and 2012AA021105) and Hong Kong Innovation and Technology Commission (GHP/043/19SZ, GHP/044/19GD)

REFERENCES

(1) Siegel, R. L.; Miller, K. D.; Jemal, A. Cancer statistics, 2020. CA Cancer J. Clin. 2020, 70, 7-30.
(2) Villanueva, A. Hepatocellular Carcinoma. N. Engl. J. Med. 2019, 380, 1450-1462.
(3) Marrero, J. A.; Kulik, L. M.; Sirlin, C. B.; Zhu, A. X.; Finn, R. S.; Abecassis, M. M.; Roberts, L. R.; Heimbach, J. K. Diagnosis, Staging, and Management of Hepatocellular Carcinoma: 2018 Practice Guidance by the American Association for the Study of Liver Diseases. Hepatology 2018, 68, 723-750.
(4) Forner, A.; Reig, M.; Bruix, J. Hepatocellular carcinoma. Lancet 2018, 391, 1301-1314.
(5) Fang, C.; Zhang, P.; Qi, X. Digital and intelligent liver surgery in the new era: Prospects and dilemmas. EBioMedicine 2019, 41, 693-701.
(6) Park, H. J.; Jang, H. Y.; Kim, S. Y.; Lee, S. J.; Won, H. J.; Byun, J. H.; Choi, S. H.; Lee, S. S.; An, J.; Lim, Y. S. Non-enhanced magnetic resonance imaging as a surveillance tool for hepatocellular carcinoma: Comparison with ultrasound. J. Hepatol. 2020, 72, 718-724.
(7) Li, C.; Zhu, A. Application of image fusion in diagnosis and treatment of liver cancer. Appl. Sci. 2020, 10, 1171.
(8) Kwee, S. A.; Wong, L.; Chan, O.; Kalathil, S.; Tsai, N. PET/CT with ^{18}F Fluorocholine as an Imaging Biomarker for Chronic Liver Disease: A Preliminary

Radiopathologic Correspondence Study in Patients with Liver Cancer. Radiology 2018, 287, 294-302.
(9) Miao, Q.; Pu, K. Organic Semiconducting Agents for Deep-Tissue Molecular Imaging: Second Near-Infrared Fluorescence, Self-Luminescence, and Photoacoustics. Adv. Mater. 2018, 30, e1801778.
(10) Lai, P.; Wang, L.; Tay, J. W.; Wang, L. V. Photoacoustically guided wavefront shaping for enhanced optical focusing in scattering media. Nat. Photonics 2015, 9, 126-132.
(11) Liu, C.; Chen, J.; Zhang, Y.; Zhu, J.; Wang, L. Five-Wavelength Optical-Resolution Photoacoustic Microscopy of Blood and Lymphatic Vessels. Adv. Photonics 2021, 3, 1–10.
(12) Liu, Y.; Nie, L.; Chen, X. Photoacoustic Molecular Imaging: From Multiscale Biomedical Applications Towards Early-Stage Theranostics. Trends Biotechnol. 2016, 34, 420-433.
(13) Zhang, Y.; Wang, L. Video-rate ring-array ultrasound and photoacoustic tomography. IEEE Trans. Med. Imaging 2020, 39, 4369-4375.
(14) Zhang, J.; Wen, G.; Wang, W.; Cheng; Guo, Q.; Tian, S.; Liu, C.; Hu, H.; Zhang, Y.; Zhang, H.; Wang, L.; Sun, H. Controllable Cleavage of C-N Bond-Based Fluorescent and Photoacoustic Dual-Modal Probes for the Detection of H_2S in Living Mice. ACS Appl. Bio. Mater. 2020. doi: 10.1021/acsabm.0c00413.
(15) Chen, J.; Zhang, Y.; Li, X.; Zhu, J.; Li, D.; Li, S.; Lee, C. S.; Wang, L. Confocal Visible/NIR Photoacoustic Microscopy of Tumor with Structural, Functional, and Nanoprobe Contrasts. Photonics Res. 2020, 8, 1875-1880.
(16) Yao, J.; Wang, L.; Yang, J. M.; Maslov, K. I.; Wong, T. T.; Li, L.; Huang, C. H.; Zou, J.; Wang, L. V. High-speed label-free functional photoacoustic microscopy of mouse brain in action. Nat. Methods 2015, 12, 407-410.
(17) Wei, T.; Liu, J.; Li, D.; Chen, S.; Zhang, Y.; Li, J.; Fan, L.; Guan, Z.; Lo, C. M.; Wang, L.; Man, K.; Sun, D. Development of Magnet-Driven and Image-Guided Degradable Microrobots for the Precise Delivery of Engineered Stem Cells for Cancer Therapy. Small 2020, 16, e1906908.
(18) Li, S.; Deng, Q.; Zhang, Y.; Li, X.; Wen, G.; Cui, X.; Wan, Y.; Huang, Y.; Chen, J.; Liu, Z.; Wang, L.; Lee, C. S. Rational Design of Conjugated Small Molecules for Superior Photothermal Theranostics in the NIR-II Biowindow. Adv. Mater. 2020, 32, e2001146.
(19) Yin, C.; Wen, G.; Liu, C.; Yang, B.; Lin, S.; Huang, J.; Zhao, P.; Wong, S.; Zhang, K.; Chen, X.; Li, G.; Jiang, X.; Huang, J.; Pu, K.; Wang, L.; Bian, L. Organic Semiconducting Polymer Nanoparticles for Photoacoustic Labeling and Tracking of Stem Cells in the Second Near-Infrared Window. ACS Nano 2018, 12, 12201-12211.
(20) Fu, Q.; Zhu, R.; Song, J.; Yang, H.; Chen, X. Photoacoustic Imaging: Contrast Agents and Their Biomedical Applications. Adv. Mater. 2019, 31, e1805875.
(21) Li, L.; Zhu, L.; Ma, C.; Lin, L.; Yao, J.; Wang, L.; Maslov, K.; Zhang, R.; Chen, W.; Shi, J.; Wang, L. V. Single-impulse Panoramic Photoacoustic Computed Tomography of Small-animal Whole-body Dynamics at High Spatiotemporal Resolution. Nat. Biomed. Eng. 2017, 1, 0071.
(22) Zha, M.; Lin, X.; Ni, J. S.; Li, Y.; Zhang, Y.; Zhang, X.; Wang, L.; Li, K. An Ester-Substituted Semiconducting Polymer with Efficient Nonradiative Decay Enhances NIR-II Photoacoustic Performance for Monitoring of Tumor Growth. Angew. Chem. Int. Ed. 2020, 59, 23268-23276.
(23) Deng, H.; Shang, W.; Lu, G.; Guo, P.; Ai, T.; Fang, C.; Tian, J. Targeted and Multifunctional Technology for Identification between Hepatocellular Carcinoma and

Liver Cirrhosis. ACS Appl. Mater. Interfaces 2019, 11, 14526-14537.
(24) Liu, Y.; Liu, H.; Yan, H.; Liu, Y.; Zhang, J.; Shan, W.; Lai, P.; Li, H.; Ren, L.; Li, Z.; Nie, L. Aggregation-Induced Absorption Enhancement for Deep Near-Infrared II Photoacoustic Imaging of Brain Gliomas *In Vivo*. Adv. Sci. 2019, 6, 1801615.
(25) Li, B.; Lu, L.; Zhao, M.; Lei, Z.; Zhang, F. An Efficient 1064 nm NIR-II Excitation Fluorescent Molecular Dye for Deep-Tissue High-Resolution Dynamic Bioimaging. Angew. Chem. Int. Ed. 2018, 57, 7483-7487.
(26) Yin, C.; Li, X.; Wen, G.; Yang, B.; Zhang, Y.; Chen, X.; Zhao, P.; Li, S.; Li, R.; Wang, L.; Lee, C. S.; Bian, L. Organic semiconducting polymer amphiphile for near-infrared-II light-triggered phototheranostics. Biomaterials 2020, 232, 119684.
(27) Liu, Y.; Bhattarai, P.; Dai, Z.; Chen, X. Photothermal therapy and photoacoustic imaging via nanotheranostics in fighting cancer. Chem. Soc. Rev. 2019, 48, 2053-2108.
(28) Zhang, W.; Cai, K.; Li, X.; Zhang, J.; Ma, Z.; Foda, M. F.; Mu, Y.; Dai, X.; Han, H. Au Hollow Nanorods-Chimeric Peptide Nanocarrier for NIR-II Photothermal Therapy and Real-time Apoptosis Imaging for Tumor Theranostics. Theranostics 2019, 9, 4971-4981.
(29) Zhou, C.; Zhang, L.; Sun, T.; Zhang, Y.; Liu, Y.; Gong, M.; Xu, Z.; Du, M.; Liu, Y.; Liu, G.; Zhang, D. Activatable NIR-II Plasmonic Nanotheranostics for Efficient Photoacoustic Imaging and Photothermal Cancer Therapy. Adv. Mater. 2020, e2006532.
(30) Arvizo, R. R.; Bhattacharyya, S.; Kudgus, R. A.; Giri, K.; Bhattacharya, R.; Mukherjee, P. Intrinsic therapeutic applications of noble metal nanoparticles: past, present and future. Chem. Soc. Rev. 2012, 41, 2943-2970.
(31) Hai, P.; Qu, Y.; Li, Y.; Zhu, L.; Shmuylovich, L.; Cornelius, L. A.; Wang, L. V. Label-free high-throughput photoacoustic tomography of suspected circulating melanoma tumor cells in patients *in vivo*. J Biomed Opt 2020, 25, 1-17.
(32) Lee, H. A.; Park, E.; Lee, H. Polydopamine and Its Derivative Surface Chemistry in Material Science: A Focused Review for Studies at KAIST. Adv. Mater. 2020, 32, e1907505.
(33) Ye, Q.; Zhou, F.; Liu, W. Bioinspired catecholic chemistry for surface modification. Chem. Soc. Rev. 2011, 40, 4244-4258.
(34) Liu, Y.; Ai, K.; Lu, L. Polydopamine and its derivative materials: synthesis and promising applications in energy, environmental, and biomedical fields. Chem. Rev. 2014, 114, 5057-5115.
(35) Wang, S.; Lin, J.; Wang, Z.; Zhou, Z.; Bai, R.; Lu, N.; Liu, Y.; Fu, X.; Jacobson, O.; Fan, W.; Qu, J.; Chen, S.; Wang, T.; Huang, P.; Chen, X. Core-Satellite Polydopamine-Gadolinium-Metallofullerene Nanotheranostics for Multimodal Imaging Guided Combination Cancer Therapy. Adv. Mater. 2017, 29, 1701013.
(36) Wang, Q.; Wang, H.; Yang, Y.; Jin, L.; Liu, Y.; Wang, Y.; Yan, X.; Xu, J.; Gao, R.; Lei, P.; Zhu, J.; Wang, Y.; Song, S.; Zhang, H. Plasmonic Pt Superstructures with Boosted Near-Infrared Absorption and Photothermal Conversion Efficiency in the Second Biowindow for Cancer Therapy. Adv. Mater. 2019, 31, e1904836.
(37) Zhang, D. Y.; Zheng, Y.; Zhang, H.; Sun, J. H.; Tan, C. P.; He, L.; Zhang, W.; Ji, L. N.; Mao, Z. W. Delivery of Phosphorescent Anticancer Iridium (III) Complexes by Polydopamine Nanoparticles for Targeted Combined Photothermal-Chemotherapy and Thermal/Photoacoustic/ Lifetime Imaging. Adv. Sci.2018, 5, 1800581.
(38) Zhou, J.; Jiang, Y.; Hou, S.; Upputuri, P. K.; Wu, D.; Li, J.; Wang, P.; Zhen, X.; Pramanik, M.; Pu, K.; Duan, H. Compact Plasmonic Blackbody for Cancer Theranosis in the Near-Infrared II Window. ACS Nano 2018, 12, 2643-2651.
(39) Wen, G.; Li, X.; Zhang, Y.; Han, X.; Xu, X.; Liu, C.; Chan, K.; Lee, C. S.; Yin, C.; Bian, L.; Wang, L. Effective Phototheranostics of Brain Tumor Assisted by Near-

Infrared-II Light-Responsive Semiconducting Polymer Nanoparticles. ACS Appl. Mater. Interfaces 2020, 12, 33492-33499.
(40) Chen, J.; Zhang, Y.; He, L.; Liang, Y.; Wang, L. Wide-field polygon-scanning photoacoustic microscopy of oxygen saturation at 1-MHz A-line rate. Photoacoustics 2020, 20, 100195.
(41) Bard, A.J.; Faulkner, L.R (2001). Electrochemical Methods, Fundamentals and Applications (2nd ed.). Wiley. ISBN 9781118312803.
(42) Jia, J.; Liu, G.; Xu, W.; Tian, X.; Li, S.; Han, F.; Feng, Y.; Dong, X.; Chen, H. Fine-Tuning the Homometallic Interface of Au-on-Au Nanorods and Their Photothermal Therapy in the NIR-II Window. Angew. Chem. Int. Ed. 2020, 59, 14443-14448.
(43) Feng, W.; Han, X.; Wang, R.; Gao, X.; Hu, P.; Yue, W.; Chen, Y.; Shi, J. Nanocatalysts-Augmented and Photothermal-Enhanced Tumor-Specific Sequential Nanocatalytic Therapy in Both NIR-I and NIR-II Biowindows. Adv. Mater. 2019, 31, e1805919.
(44) Men, X.; Wang, F.; Chen, H.; Liu, Y.; Yuan, Z. Ultrasmall Semiconducting Polymer Dots with Rapid Clearance for Second Near - Infrared Photoacoustic Imaging and Photothermal Cancer Therapy. Adv. Funct. Mater. 2020, 30, 1909673.
(45) Wei, Z.; Wu, M.; Lan, S.; Li, J.; Zhang, X.; Zhang, D.; Liu, X.; Liu, J. Semiconducting polymer-based nanoparticles for photothermal therapy at the second near-infrared window. Chem. Commun. 2018, 54, 13599-13602.
(46) Lin, H.; Gao, S.; Dai, C.; Chen, Y.; Shi, J. A Two-Dimensional Biodegradable Niobium Carbide (MXene) for Photothermal Tumor Eradication in NIR-I and NIR-II Biowindows. J. Am. Chem. Soc. 2017, 139, 16235-16247.
(47) Fu, Q.; Li, Z.; Ye, J.; Li, Z.; Fu, F.; Lin, S. L.; Chang, C. A.; Yang, H.; Song, J. Magnetic targeted near-infrared II PA/MR imaging guided photothermal therapy to trigger cancer immunotherapy. Theranostics 2020, 10, 4997-5010.
(48) Yin, W.; Bao, T.; Zhang, X.; Gao, Q.; Yu, J.; Dong, X.; Yan, L.; Gu, Z.; Zhao, Y. Biodegradable MoO_x nanoparticles with efficient near-infrared photothermal and photodynamic synergetic cancer therapy at the second biological window. Nanoscale 2018, 10, 1517-1531.
(49) Yu, X.; Li, A.; Zhao, C.; Yang, K.; Chen, X.; Li, W. Ultrasmall Semimetal Nanoparticles of Bismuth for Dual-Modal Computed Tomography/Photoacoustic Imaging and Synergistic Thermoradiotherapy. ACS Nano 2017, 11, 3990-4001.
(50) Zhu, P.; Gao, S.; Lin, H.; Lu, X.; Yang, B.; Zhang, L.; Chen, Y.; Shi, J. Inorganic Nanoshell-Stabilized Liquid Metal for Targeted Photonanomedicine in NIR-II Biowindow. Nano Lett. 2019, 19, 2128-2137.
(51) Liu, G.; Zhu, J.; Guo, H.; Sun, A.; Chen, P.; Xi, L.; Huang, W.; Song, X.; Dong, X. Mo_2C-Derived Polyoxometalate for NIR-II Photoacoustic Imaging-Guided Chemodynamic/Photothermal Synergistic Therapy. Angew. Chem. Int. Ed. 2019, 58, 18641-18646.
(52) Liu, H.; Liu, Y.; Liu, W.; Zhang, W.; Xu, J. EZH2-mediated loss of miR-622 determines CXCR4 activation in hepatocellular carcinoma. Nat. Commun. 2015, 6, 8494.
(53) Li, M.; Lu, Y.; Xu, Y.; Wang, J.; Zhang, C.; Du, Y.; Wang, L.; Li, L.; Wang, B.; Shen, J.; Tang, J.; Song, B. Horizontal transfer of exosomal CXCR4 promotes murine hepatocarcinoma cell migration, invasion and lymphangiogenesis. Gene 2018, 676, 101-109.
(54) Gao, D. Y.; Lin, T. T.; Sung, Y. C.; Liu, Y. C.; Chiang, W. H.; Chang, C. C.; Liu, J. Y.; Chen, Y. CXCR4-targeted lipid-coated PLGA nanoparticles deliver sorafenib and overcome acquired drug resistance in liver cancer. Biomaterials 2015, 67, 194-203.

(55) Huang, X.; Shang, W.; Deng, H.; Zhou, Y.; Cao, F.; Fang, C.; Lai, P.; Tian, J. Clothing spiny nanoprobes against the mononuclear phagocyte system clearance *in vivo*: Photoacoustic diagnosis and photothermal treatment of early stage liver cancer with erythrocyte membrane-camouflaged gold nano stars. Appl. Mater. Today 2020, 18, 100484.
(56) Wilhelm, S.; Tavares, A. J.; Qin, D.; Ohta, S.; Chan, W. C. W. Analysis of nanoparticle delivery to tumours. Nat. Rev. Mater. 2016, 1, 16014.
(57) Sun, T.; Han, J.; Liu, S.; Wang, X.; Wang, Z. Y.; Xie, Z. Tailor-Made Semiconducting Polymers for Second Near-Infrared Photothermal Therapy of Orthotopic Liver Cancer. ACS Nano 2019, 13, 7345-7354.
(58) Li, Q.; Chen, K.; Huang, W.; Ma, H.; Zhao, X.; Zhang, J.; Zhang, Y.; Fang, C.; Nie, L. Minimally invasive photothermal ablation assisted by laparoscopy as an effective preoperative neoadjuvant treatment for orthotopic hepatocellular carcinoma. Cancer Lett. 2021, 496, 169-178.
(59) Li, X.; Lovell, J. F.; Yoon, J.; Chen, X. Clinical development and potential of photothermal and photodynamic therapies for cancer. Nat. Rev. Clin. Oncol. 2020, 17, 657-674.

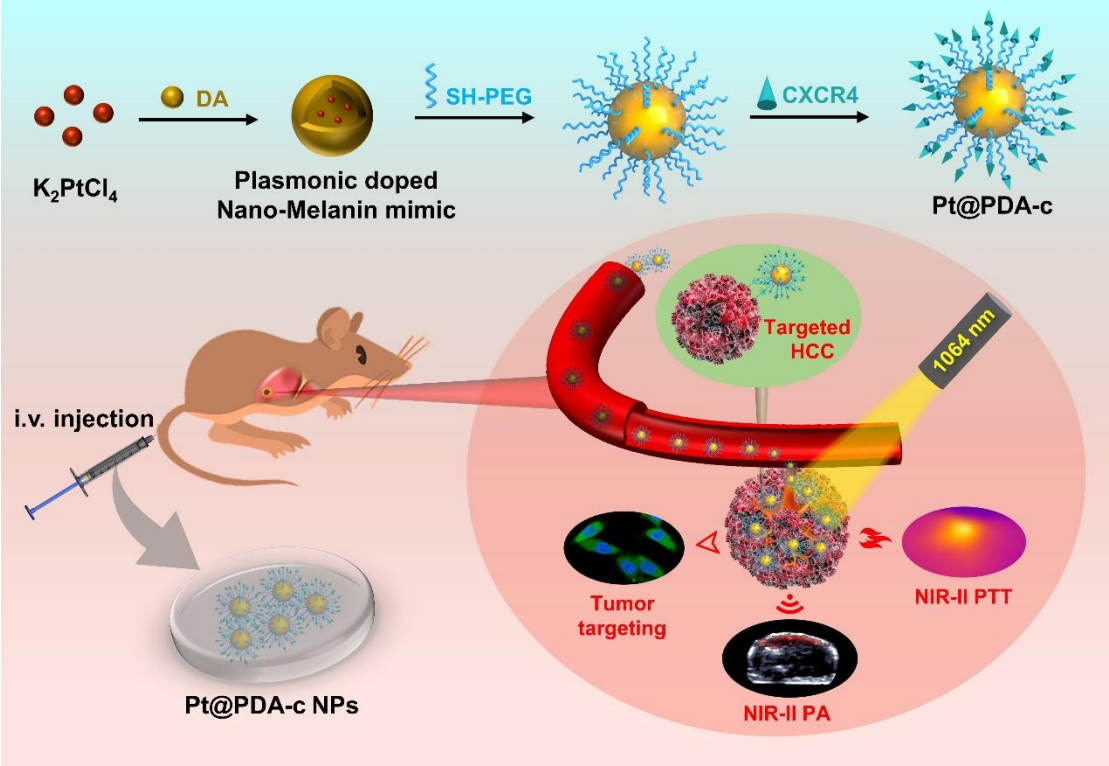

Scheme 1 Preparation of Pt@PDA-c nanoparticles and their applications in PACT-guided PTT for orthotopic HCC bearing nude mice.

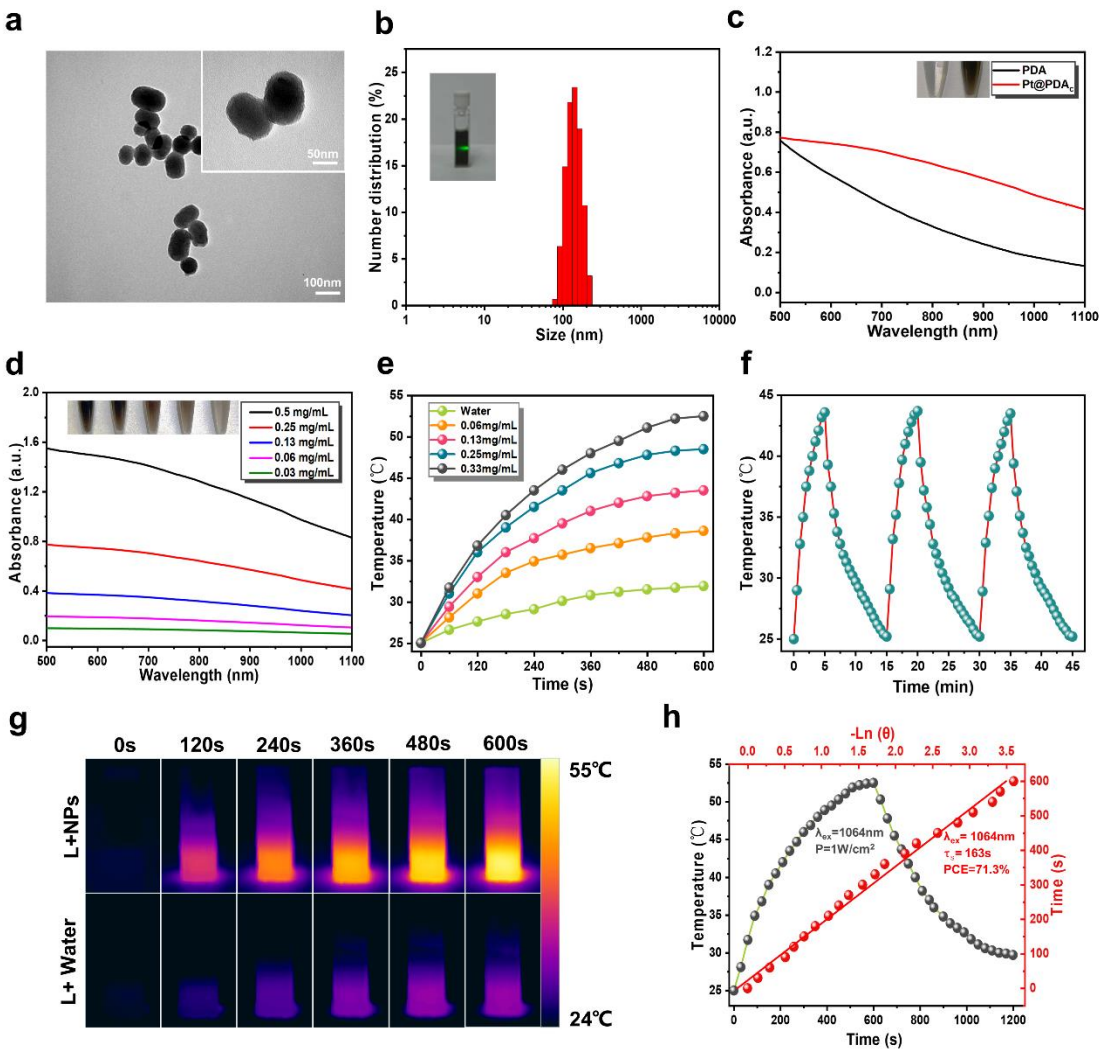

Figure 1 a) TEM images of Pt@PDA-c. b) DLS size distribution of Pt@PDA-c NPs (inset: digital photo of dispersion with typical Tyndall effect). c) UV-Vis spectra of PDA and Pt@PDA-c aqueous solution. Inset: Photographs of PDA and Pt@PDA-c aqueous solution (from left to right). d) UV-Vis spectra of Pt@PDA-c aqueous dispersions at different concentrations. Inset: Photographs of the NPs in dispersions of different concentrations from 0.03, 0.06, 0.13, 0.25 and 0.5 mg mL^{-1} (from right to left). e) Temperature elevation curves of Pt@PDA-c at different concentrations during laser irradiation (1064 nm, 1 $W \cdot cm^{-2}$). f) Photothermal heating & cooling cycles of Pt@PDA-c (0.25 mg mL^{-1}) upon 1064-nm laser irradiation (1 $W \cdot cm^{-2}$). g) Infrared thermal images of Pt@PDA-c (0.33 mg mL^{-1}) and DI water in quartz cuvettes upon 1064-nm laser irradiation of 1 $W \cdot cm^{-2}$ for 10 minutes. h) Full heating & cooling profile and linear regression for determination of time constant τ_s.

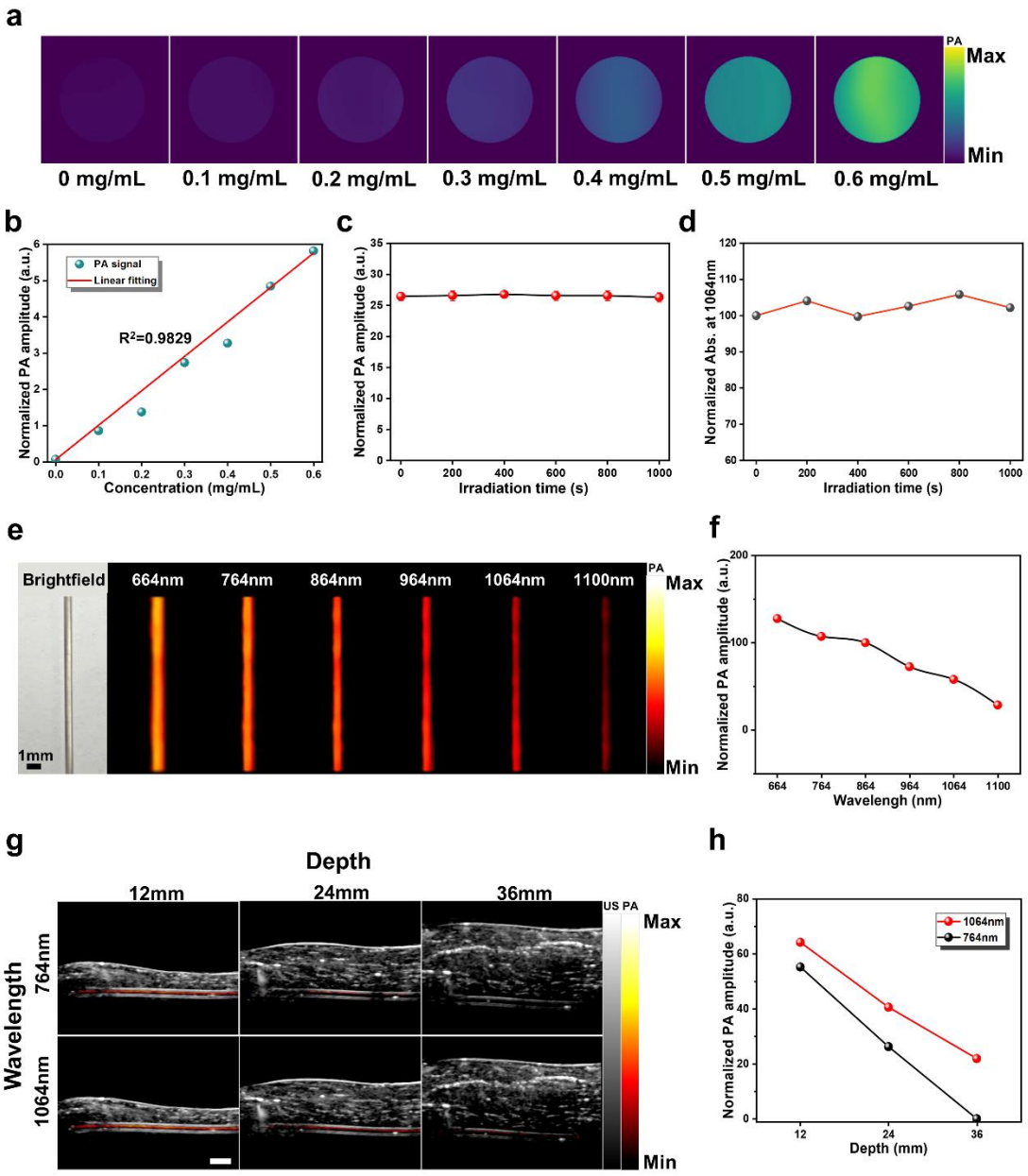

Figure 2 a) Concentration dependent PA images of Pt@PDA-c dispersions (Laser energy: 8 mJ·cm^{-2} at 1064 nm). b) The corresponding linear regression curve of PA intensity against concentrations of Pt@PDA-c. c) PA signal stability test of Pt@PDA-c under 1064-nm laser irradiation for 1000 seconds. d) Absorption of Pt@PDA-c at 1064 nm with continuous laser irradiation (8 mJ·cm^{-2}). e) PA images of a capillary tube filled with Pt@PDA-c (0.5 mg mL^{-1}) under laser irradiation of different wavelengths. f) Corresponding quantitative curve of PA intensity at different wavelengths. g) Superimpose images of ultrasound (black & white) and PA signal (red) with varied thickness of chicken breast tissue coverage under 764 nm (upper row) or 1064 nm (lower row) (energy density: 9.5mJ·cm^{-2}), bar:10 mm. h) The corresponding PA intensity from (G) as a function of tissue depth.

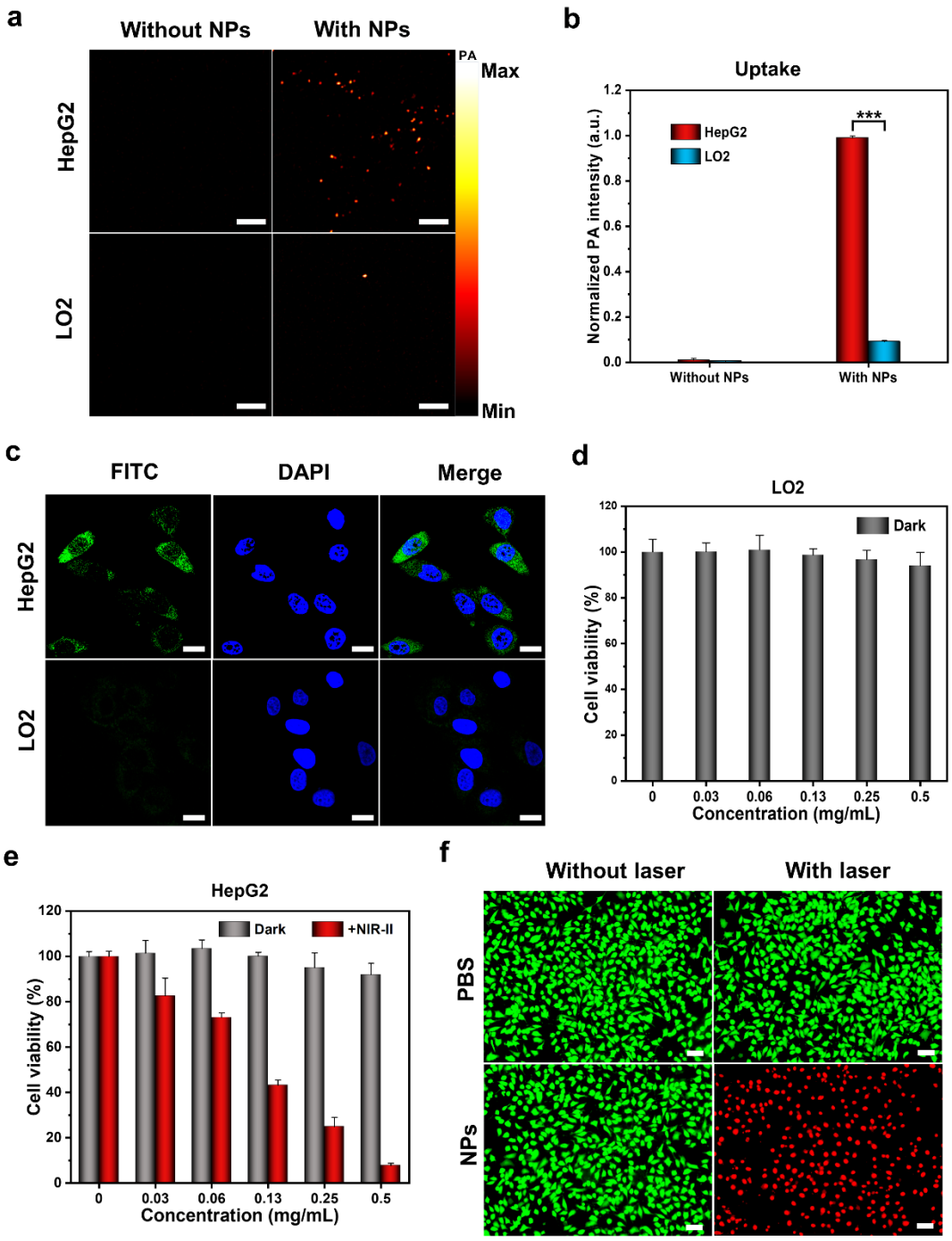

Figure 3 a) PA microscopy scanning for HepG2 and LO2 cells treated with Pt@PDA-c (scale bar: 100 μm). b) Normalized PA intensity of HepG2 and LO2 cells with or without Pt@PDA-c, ***P<0.001. c) CLSM images for Pt@PDA-c uptake in HepG2 and LO2 cells (scale bar: 20 μm). d) Cell viability of LO2 cells after incubation with Pt@PDA-c NPs of different concentrations in dark for 24 hours. e) Cell viability of HepG2 cells after incubation with Pt@PDA-c NPs of different concentrations in dark or with laser irradiation (1064 nm, 1 $W \cdot cm^{-2}$). f) Calcein AM (green, for live cells) and PI (red, for dead cells) double staining images, (scale bar: 100 μm).

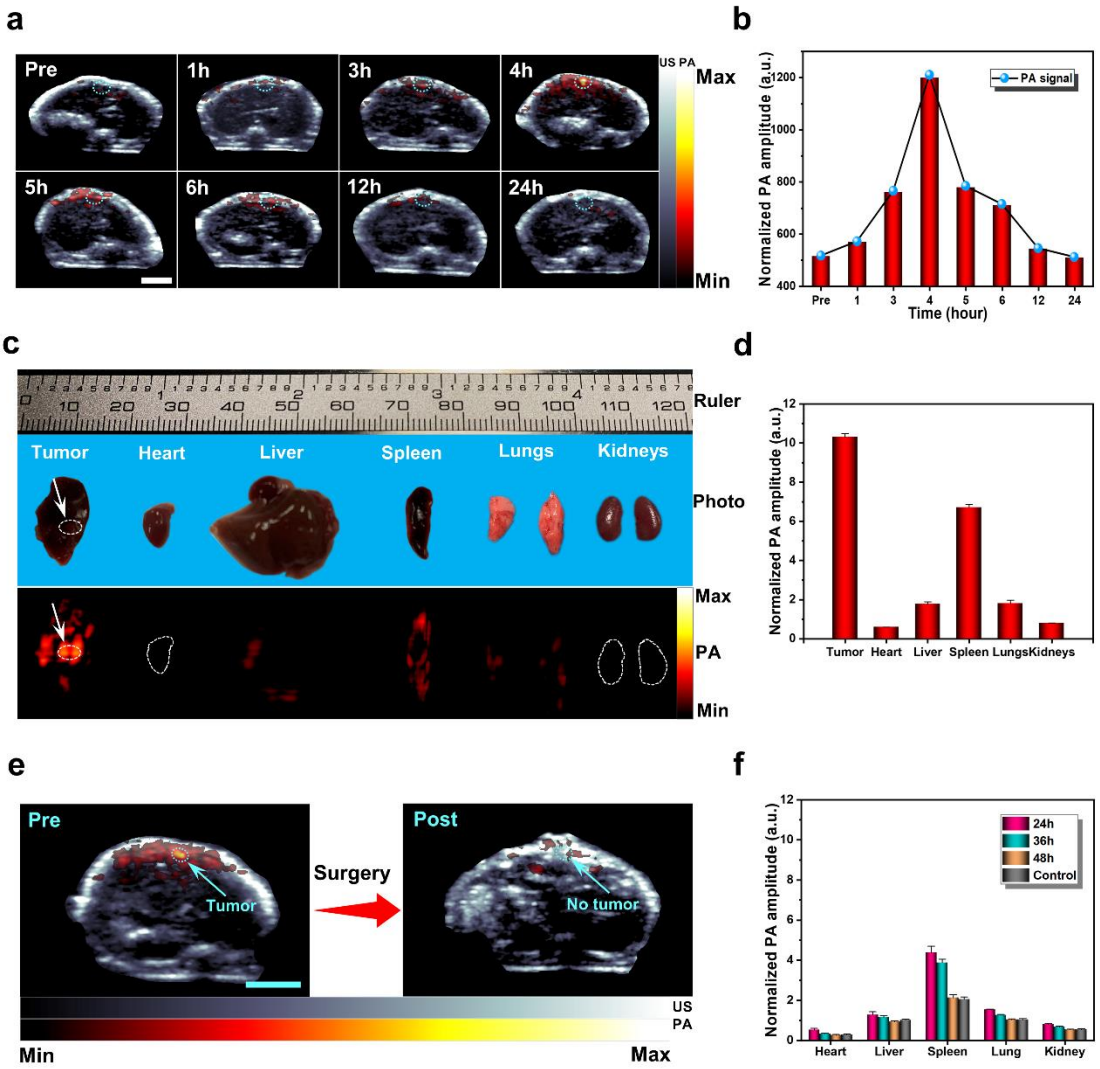

Figure 4 a) *In vivo* NIR-II PACT imaging of the tumor at different post injection time points of Pt@PDA-c (scale bar: 5 mm). b) Corresponding quantification of PA signal at tumor site. c) *Ex vivo* MAP PA images of the liver tumor and major organs at 4 hours after injection of NPs. d) Quantification of mean PA signal from c). e). Preoperative and postoperative PACT imaging of the liver tumor at 4 hours post-injection (scale bar: 5 mm). f) The PA signal from the major organs of tumor-free mice at 24, 36, and 48 hours post-injection.

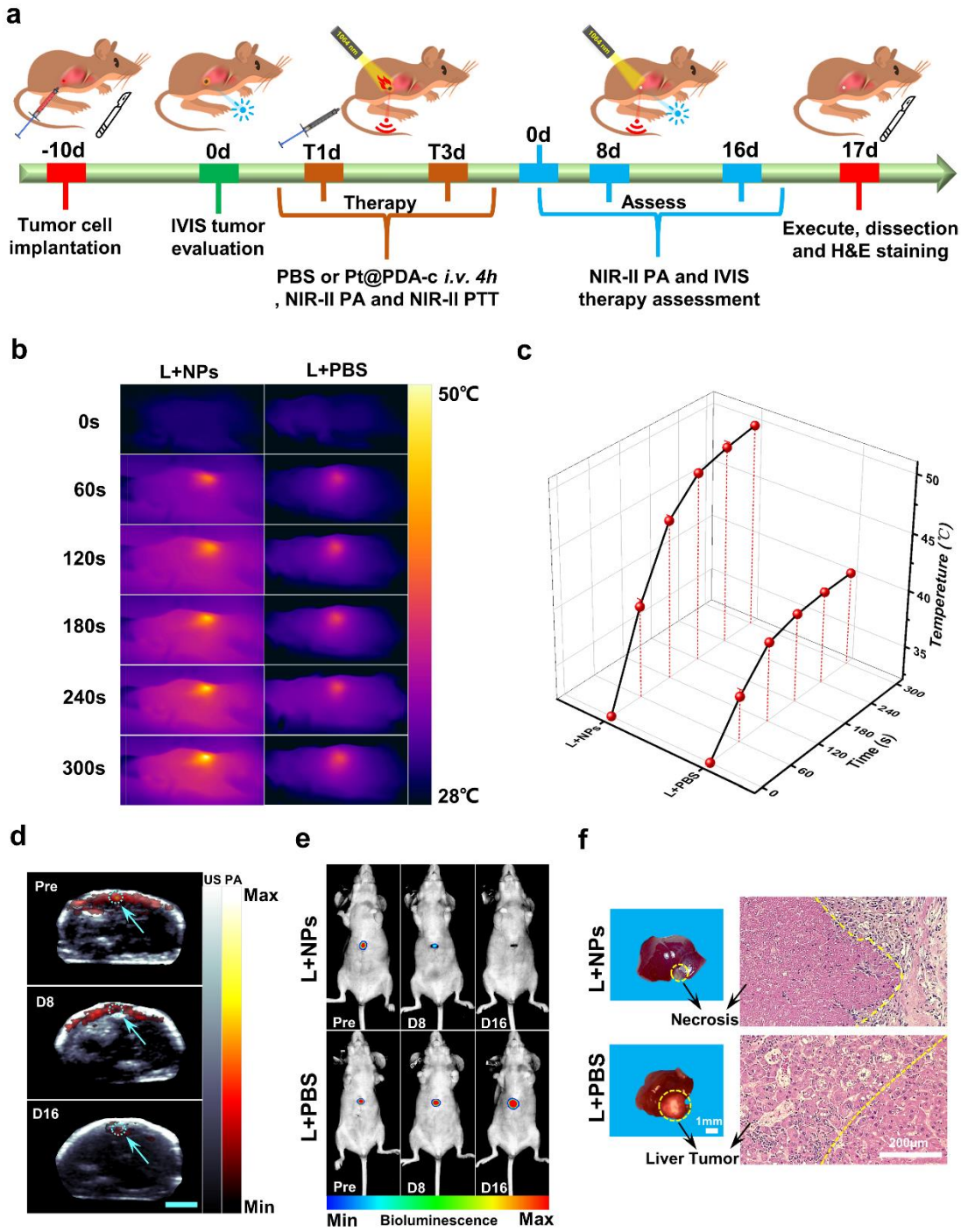

Figure 5 a) The detailed process of NIR-II PACT-guided PTT and efficacy evaluation for orthotopic tumor bearing nude mice. b) Infrared thermal imaging of HepG2-tumor-bearing mice treated respectively with PBS and Pt@PDA-c upon 1064-nm laser (1 $W \cdot cm^{-2}$) irradiation for different durations, respectively. c) Heating curves of tumor-site upon laser irradiation. d) PACT for monitoring of orthotopic HCC before and after treatment (Pre, day 8 and day 16), the scale bar is 5 mm. e) Continuous monitoring of orthotopic HCC fluorescence signals by bioluminescence imaging before and after treatment (Pre, day 8 and day 16). f) Photograph of tumors after different treatments with corresponding H&E staining.

Table of Contents Graphic